Lithos 232 (2015) 306–318

Contents lists available at ScienceDirect

Lithos

journal homepage: www.elsevier.com/locate/lithos

Mid-Cretaceous oblique rifting of West Antarctica: Emplacement and rapid cooling of the Fosdick Mountains migmatite-cored gneiss dome

R.R. McFadden [a,*], C. Teyssier [b], C.S. Siddoway [c], M.A. Cosca [d], C.M. Fanning [e]

[a] Department of Geological Sciences, Salem State University, 352 Lafayette St., Salem, MA 01970, USA
[b] Department of Earth Sciences, University of Minnesota, Minneapolis, MN 55455, USA
[c] Department of Geology, Colorado College, Colorado Springs, CO 80903, USA
[d] U.S. Geological Survey, Denver Federal Center, MS 963, Denver, CO 80225, USA
[e] Research School Earth Sciences, Australian National University, Canberra, ACT 0200, Australia

ARTICLE INFO

Article history:
Received 2 December 2014
Accepted 8 July 2015
Available online 26 July 2015

Keywords:
$^{40}Ar/^{39}Ar$ thermochronology
Rapid cooling
Gneiss domes
Detachments
Migmatites

ABSTRACT

In Marie Byrd Land, West Antarctica, the Fosdick Mountains migmatite-cored gneiss dome was exhumed from mid- to lower middle crustal depths during the incipient stage of the West Antarctic Rift system in the mid-Cretaceous. Prior to and during exhumation, major crustal melting and deformation included transfer and emplacement of voluminous granitic material and numerous intrusions of mantle-derived diorite in dikes. A succession of melt- and magma-related structures formed at temperatures in excess of 665 ± 50 °C based on Ti-in-zircon thermometry. These record a transition from wrench to oblique extensional deformation that culminated in the development of the oblique South Fosdick Detachment zone. Solid-state fabrics within the detachment zone and overprinting brittle structures record translation of the detachment zone and dome to shallow levels.

To determine the duration of exhumation and cooling, we sampled granite and gneisses at high spatial resolution for U–Pb zircon geochronology and $^{40}Ar/^{39}Ar$ hornblende and biotite thermochronology. U–Pb zircon crystallization ages for the youngest granites are 102 Ma. Three hornblende ages are 103 to 100 Ma and 12 biotite ages are 101 to 99 Ma. All overlap within uncertainty. The coincidence of zircon crystallization ages with $^{40}Ar/^{39}Ar$ cooling ages indicates cooling rates >100 °C/m.y. that, when considered together with overprinting structures, indicates rapid exhumation of granite and migmatite from deep to shallow crustal levels within a transcurrent setting. Orientations of structures and age-constrained crosscutting relationships indicate counterclockwise rotation of stretching axes from oblique extension into nearly orthogonal extension with respect to the Marie Byrd Land margin. The rotation may be a result of localized extension arising from unroofing and arching of the Fosdick dome, extensional opening within a pull-apart zone, or changes in plate boundary configuration.

The rapid tectonic and temperature evolution of the Fosdick Mountains dome lends support to recently developed numerical models of crustal flow and cooling in orogenic crust undergoing extension/transtension, and accords with numerous studies of migmatite-cored gneiss domes in transcurrent settings.

1. Introduction

Extension of thickened and hot crust commonly leads to the formation of migmatite-cored metamorphic core complexes (MCC) (Coney and Harms, 1984; Lister and Davis, 1989; Whitney et al., 2004, 2013). Within these crustal-scale structures, detachment zones record significant amounts of localized extension and preserve an interface between cool upper crust and hot middle to lower crust (Lister and Davis, 1989; Malavieille, 1993; Mulch et al., 2006). Studies in the Basin and Range (e.g. Crittenden et al., 1980), the northern Cordillera (USA and Canada) (e.g. Foster et al., 2001; Vanderhaeghe et al., 1999), and the Aegean region (e.g. Brichau et al., 2008; Denele et al., 2011) have shown a spatial and temporal link between extensional detachment tectonics and the emplacement of gneiss/migmatite domes and granite bodies. Field, thermochronologic, and numerical modeling studies suggest the intrusion of granites may initiate the formation of detachment zones (e.g. Foster et al., 2001; Lister and Baldwin, 1993; Tirel et al., 2006, 2008) and the presence of a low-viscosity layer in the crust (partially molten) may enhance strain localization and the development of rolling-hinge detachment systems (Whitney et al., 2013).

In extending orogens, regions with migmatite-cored gneiss domes and MCCs typically record cooling rates that range from 30 °C/m.y. to >100 °C/m.y. where granite intrusion and detachments may be linked (Whitney et al., 2013). This includes areas such as the northern Cordilleran core complexes (Fayon et al., 2004; Foster et al., 2001; Gordon et al., 2008; Kruckenberg et al., 2008; Norlander et al., 2002), the Basin and Range province (Foster et al., 1990, 1992), the Liaodong

* Corresponding author.
E-mail address: rmcfadden@salemstate.edu (R.R. McFadden).

http://dx.doi.org/10.1016/j.lithos.2015.07.005
0024-4937/

Peninsula in NE China (Charles et al., 2012; Yang et al., 2007), and the Aegean domain (Brichau et al., 2008; Lister et al., 1984). In addition, recent thermomechanical numerical models have shown that gneiss domes are exhumed over short timescales (a few m.y.) in cases of localized extension (Rey et al., 2009a, 2009b). These systems are characterized by localized upper crustal deformation, isothermal decompression, advection of heat (solidus) toward the surface, and crystallization of partially molten crust at shallow depths (Rey et al., 2009a, 2009b; Whitney et al., 2013).

In order to evaluate the timing of detachment tectonics, cooling, and exhumation of the Fosdick dome, we present new $^{40}Ar/^{39}Ar$ hornblende and biotite data combined with previously obtained U–Pb data on zircon, titanite, and monazite, $^{40}Ar/^{39}Ar$ data on hornblende, biotite, muscovite, and K-feldspar, and fission-track data on apatite from the Fosdick Mountains region. The new $^{40}Ar/^{39}Ar$ data clarify the Fosdick dome history from emplacement to cooling, expand understanding of the significant thermal event in the mid-Cretaceous West Antarctic region, assess the mid-crustal response to the initiation of West Antarctic rifting, and inform the cooling history of gneiss domes and MCCs.

2. Geologic setting

Cretaceous extension and crustal heating affected the wide accretionary zone developed in Paleozoic–Mesozoic time along the East Gondwana margin of West Antarctica and Zealandia (Davey and Brancolini, 1995; Luyendyk, 1995; Mortimer et al., 2006; Siddoway, 2008; Tulloch et al., 2006). A Jurassic–Cretaceous magmatic arc developed along the West Antarctica–Zealandia margin (Bradshaw et al., 1997; Mortimer et al., 1999). The magmatic arc included emplacement of the subduction-related Median Batholith in New Zealand at ca. 145–120 Ma (Mortimer et al., 1999; Muir et al., 1997, 1998; Tulloch and Kimbrough, 2003). Inboard of the magmatic arc, extension led to the formation of core complexes in South Island, New Zealand (Forster and Lister, 2003; Tulloch and Kimbrough, 1989), shear zones in Fiordland (Gibson et al., 1988; Scott and Cooper, 2006), oblique detachment structures in the Fosdick Mountains (McFadden et al., 2007), and detachment structures in the Ross Sea (Fitzgerald and Baldwin, 1997; Siddoway et al., 2004a). U–Pb ages record high temperature metamorphism and crustal melting within gneisses in Fiordland, New Zealand, at ca. 126–100 Ma (Flowers et al., 2005; Hollis et al., 2004; Ireland and Gibson, 1998; Scott and Cooper, 2006), and in the Paparoa metamorphic core complex, New Zealand, at ca. 119–109 Ma (Ireland and Gibson, 1998; Kimbrough and Tulloch, 1989). Migmatites of the Fosdick Mountains preserve U–Pb zircon ages ranging from ca. 117 to 102 Ma (Korhonen et al., 2010b; McFadden et al., 2010a, 2010b; Yakymchuk et al., 2013a). In addition, back-arc related alkalic plutons, represented by the Byrd Coast Granite in the Ford Ranges, were emplaced from ca. 119 to 103 Ma (Korhonen et al., 2010b; Siddoway et al., 2004a; Weaver et al., 1992, 1994).

In western Marie Byrd Land, rock exposures in the Ford Ranges display evidence for the formation of the West Antarctic Rift system (WARS) (Fig. 1) (Luyendyk et al., 2003; Siddoway, 2008; Siddoway et al., 2004a, 2005; Storey et al., 1999). Mafic dikes that strike NNW–SSE have $^{40}Ar/^{39}Ar$ ages of ca. 142–96 Ma (Luyendyk et al., 2003; Richard et al., 1994; Siddoway et al., 2005; Storey et al., 1999). Brittle normal faults strike NW–SE; dextral oblique minor faults and sinistral shear fractures strike NE. Aeromagnetic and airborne gravity data identify a conjugate geometry of ~E–W-oriented dextral and NE–SW-oriented sinistral strike–slip faults that are mutually crosscutting with the mafic dikes (Ferraccioli et al., 2002; Luyendyk et al., 2003). These structures record ENE–WSW dextral transtension over a >1000 km^2 area in the eastern WARS (Siddoway, 2008; Siddoway et al., 2005). Within Marie Byrd Land, an E–W-striking dextral transform fault is inferred to separate the Ross continental province, which contains the Ford Ranges, from the Amundsen magmatic arc province (Fig. 1A) (Pankhurst et al., 1998). In the Fosdick Mountains, migmatites and granites that experienced melt-present deformation between ca. 117 and 102 Ma also record ENE–WSW stretching suggesting kinematics in the deep crust are consistent with upper crustal structures (McFadden et al., 2007, 2010a,2010b; Siddoway et al., 2004b).

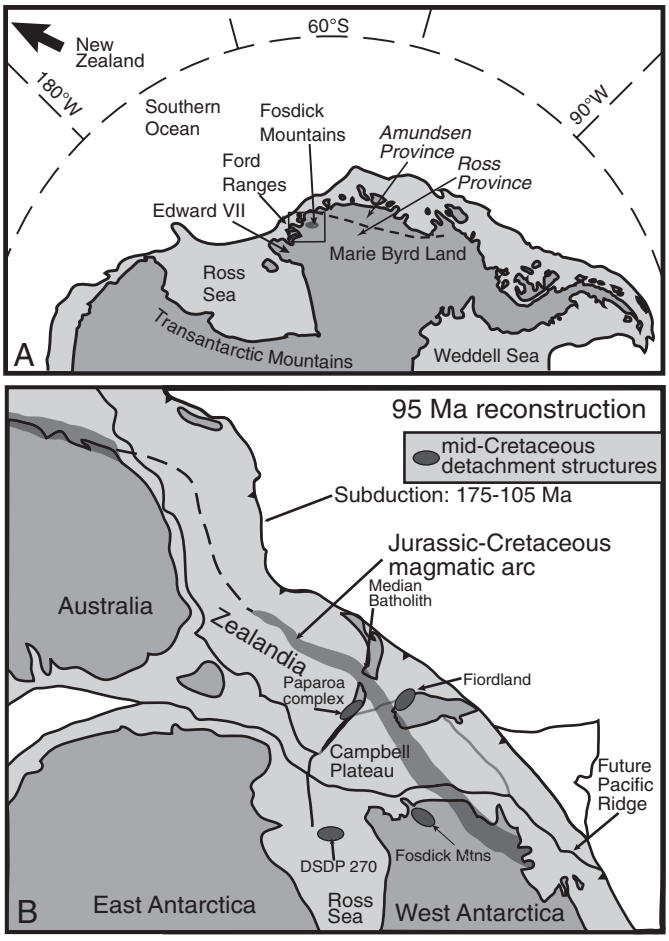

Fig. 1. (A) Geographic map of West Antarctica after Pankhurst et al. (1998). (B) Tectonic reconstruction of Antarctica–Zealandia (New Zealand + oceanic plateaus)–Australia at 95 Ma. Modified from Tulloch et al. (2006) and from McFadden et al. (2010b). DSDP = Deep Sea Drilling Project core.

$^{40}Ar/^{39}Ar$ ages in the Fosdick Mountains record cooling between ca. 103 to 95 Ma, whereas the Ford Granodiorite at Mt. June and Lewis Rocks in the Phillips Mountains preserve $^{40}Ar/^{39}Ar$ hornblende and biotite cooling ages of ~350 Ma (Fig. 2) (Richard et al., 1994). In addition, gravity data show differences in crustal thickness between the Fosdick and Phillips Mountains (Luyendyk et al., 2003). The change in crustal thickness and distinct thermal histories led to the inference of the crustal-scale Balchen Glacier fault along the northern boundary of the Fosdick Mountains (Siddoway et al., 2004b).

The rocks in western Marie Byrd Land consist of lower Paleozoic Swanson Formation metagraywacke and Devonian Ford Granodiorite (Bradshaw et al., 1983; Pankhurst et al., 1998). Cretaceous alkalic granites, represented by the Byrd Coast Granite, as well as mafic dikes intruded the Paleozoic rocks (Saito et al., 2013; Siddoway et al., 2005; Storey et al., 1999; Weaver et al., 1992). The Swanson Formation and the Ford Granodiorite are the sources for the migmatites in the Fosdick Mountains (Korhonen et al., 2010b, 2011; Siddoway and Fanning, 2009; Yakymchuk et al., 2013a). In the Paleozoic, the plutonic and metasedimentary rocks experienced granulite facies metamorphism at 820–870 °C and 7–12 kbar, and in the mid-Cretaceous, the migmatites experienced high temperature metamorphism and voluminous crustal melting at 830–865 °C and 6–7.5 kbar (Korhonen et al., 2010a).

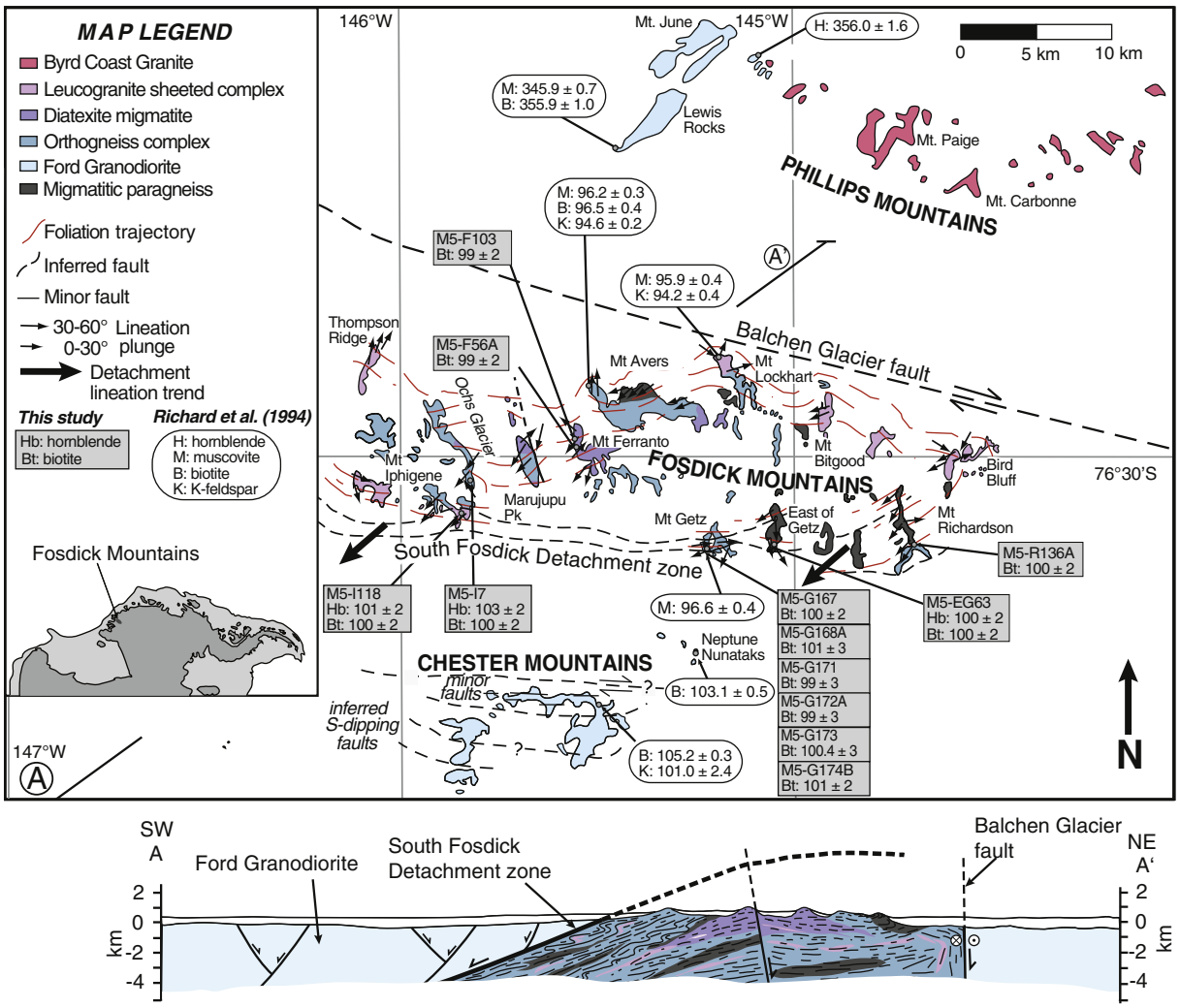

Fig. 2. Geologic map and cross-section of Fosdick Mountains (after McFadden et al., 2010b). Location of the Fosdick Mountains in Marie Byrd Land, Antarctica, is shown in the map legend. Large arrows represent the lineation trend within the migmatites and granites. Long dashed lines represent the mapped foliation trajectories. U–Pb SHRIMP zircon and titanite ages from previous studies (Korhonen et al., 2010b; McFadden et al., 2010b), $^{40}Ar/^{39}Ar$ data from Richard et al. (1994) and $^{40}Ar/^{39}Ar$ hornblende and biotite data presented in this study are shown on the map.

The elevated crustal isotherms and crustal melting in the Cretaceous are attributed to moderate thickening followed by lithospheric thinning and underplating of mafic magma during WARS-related extension (Mukasa and Dalziel, 2000; Siddoway, 2008; Weaver et al., 1994). Within the Fosdick Mountains, mafic dikes and a diorite pluton have U–Pb zircon crystallization ages ranging from ca. 113 to 98 Ma (Saito et al., 2013). The mafic dikes have positive εSr values and negative to slightly positive εNd values that suggest a melt source consisting of metasomatized sub-arc mantle that may have experienced decompression melting (Saito et al., 2013). Late discordant granites have the most juvenile εHf(t) and lowest $\delta^{18}O$ isotopic ratios, which suggests a more mantle-rich source likely caused by lithospheric thinning during the initiation of oblique extension and ultimately the establishment of regional orthogonal extension (Yakymchuk et al., 2013a).

Tectonic reconstructions in Marie Byrd Land along the tectonic boundary between the Amundsen magmatic arc province and the Ross continental province place the magmatic arc directly outboard of the Ford Ranges (Siddoway, 2008). The restored position of the magmatic arc locates a heat source that would have affected the Ross province, causing widespread regional heating, elevated geothermal gradients, mid-crustal flow, rapid extension across WARS, and lack of an orogenic plateau (Siddoway, 2008). The U–Pb zircon ages as young as 102 Ma for the Fosdick dome are consistent with Byrd Coast Granite ages of ca. 106–105 Ma for the broader Ford Ranges and Edward VII Peninsula (Korhonen et al., 2010b; Siddoway et al., 2004a; Weaver et al., 1992, 1994) suggesting that the entire West Antarctic region was undergoing a period of substantial magmatic activity. These ages of ca. 100 Ma tie the West Antarctic thermal event to the Circum-Pacific superplume (Vaughan, 1995). The West Antarctic event may also clarify the major decrease in erosion rate in mid-Cretaceous time that is recorded by detrital geochronology on moraine and other sediment in East Antarctica (Thomson et al., 2013). In addition, apatite fission-track ages for the Ford Ranges and Edward VII Peninsula range from ca. 91 to 88 Ma, indicating the entire region underwent a similar thermal evolution. In contrast, the Fosdick apatite fission track ages range from ca. 86 to 67 Ma, which suggests that Fosdick dome may provide additional information for the thermal evolution of West Antarctica.

3. Fosdick Mountains migmatite-cored gneiss dome

The Fosdick Mountains preserve lithologies and structures associated with the Devonian-Carboniferous and Cretaceous crustal melting and deformation episodes. Cretaceous granites and migmatites are more voluminous than Devonian-Carboniferous granites and migmatites in the Fosdick Mountains and most fabrics and structures

record Cretaceous deformation. However, kilometer-scale domains of migmatitic paragneiss, migmatitic orthogneiss, and granites associated with Devonian-Carboniferous crustal melting and deformation are preserved (Korhonen et al., 2010a,2010b; Siddoway and Fanning, 2009; Yakymchuk et al., 2013b). The Devonian-Carboniferous event led to the formation of the Fosdick migmatite–granite complex (Korhonen et al., 2010a,2010b, 2011; Siddoway and Fanning, 2009; Yakymchuk et al., 2013a), whereas the Cretaceous crustal melting and subsequent exhumation is referred to as a migmatite-cored gneiss dome (McFadden et al., 2010a, 2010b; Siddoway, 2008; Siddoway et al., 2004b). The presence of a migmatite–granite complex prior to Cretaceous crustal melting and gneiss dome formation provided lithologic heterogeneity and anisotropic crust.

The deepest portions of the Fosdick dome consist of an ~5 km-thick sequence of subhorizontal layers of predominantly Cretaceous migmatitic paragneiss and orthogneiss, and diatexite migmatite (Fig. 3C) that are folded into kilometer-scale recumbent folds. An ~2 km-thick sequence of Cretaceous subhorizontal leucogranite sheets up to 100 m-thick overlie the migmatitic paragneisses and orthogneisses. Dioritic dikes and sills transect the Fosdick dome rocks. Dikes and sills are folded, stretched, or interfoliated with the Cretaceous gneissic foliation, depending on their timing of emplacement, orientation, and position in the dome (Fig. 3A, C). The Fosdick migmatites also contain nodular, granular-textured patches of cordierite with K-feldspar and quartz that overprint foliation and preserve biotite-free rims, which are associated with near-isothermal decompression (Siddoway et al., 2004b).

The South Fosdick Detachment zone (SFD), a shallowly dipping, dextral oblique structure, bounds the southern portion of the Fosdick Mountains (McFadden et al., 2007). The Balchen Glacier fault, an inferred strike–slip fault, forms the northern boundary of the Fosdick Mountains (Fig. 2) (Siddoway et al., 2004b, 2005). In the Fosdick dome, Cretaceous gneissic foliations define an elongate domal shape. Foliations are predominantly subhorizontal, however, 100 m- to km-scale domains of subvertical to steeply dipping layering and foliation are also preserved (McFadden et al., 2010a,2010b). The steeply dipping foliation domains are cut by, and commonly transposed into zones of subhorizontal foliation (McFadden et al., 2010a; Siddoway et al., 2004b). Lineations and fold hinge lines trend predominantly NE–SW. It has been proposed that the overprinting and transposition of steep foliation correspond to a transition from wrench deformation to oblique extension, and that the lineation orientation represents the maximum finite stretching axis recorded in the mid-crust (McFadden et al., 2010b).

The SFD zone is an ~1 km-thick zone of solid-state sheared migmatitic gneisses with penetrative foliation and lineation (Figs. 3B and4A) (McFadden et al., 2007). In the eastern Fosdick Mountains, the boundary of the SFD-leucogranite sheeted complex is gradational, corresponding to a decrease upward in the proportion of leucogranite sheets and an increase in the prevalence of solid-state deformation. This description highlights that the SFD zone is the base of a detachment zone, with the upper portions of the detachment either eroded or covered by ice.

During Cretaceous crustal melting, three generations of granite were emplaced in distinct structural settings. Granites were emplaced as subvertical layers between ca. 117 and 114 Ma. Granites accumulated as voluminous subhorizontal sheets below and within the South Fosdick Detachment zone between ca. 109 and 102 Ma. Structurally discordant

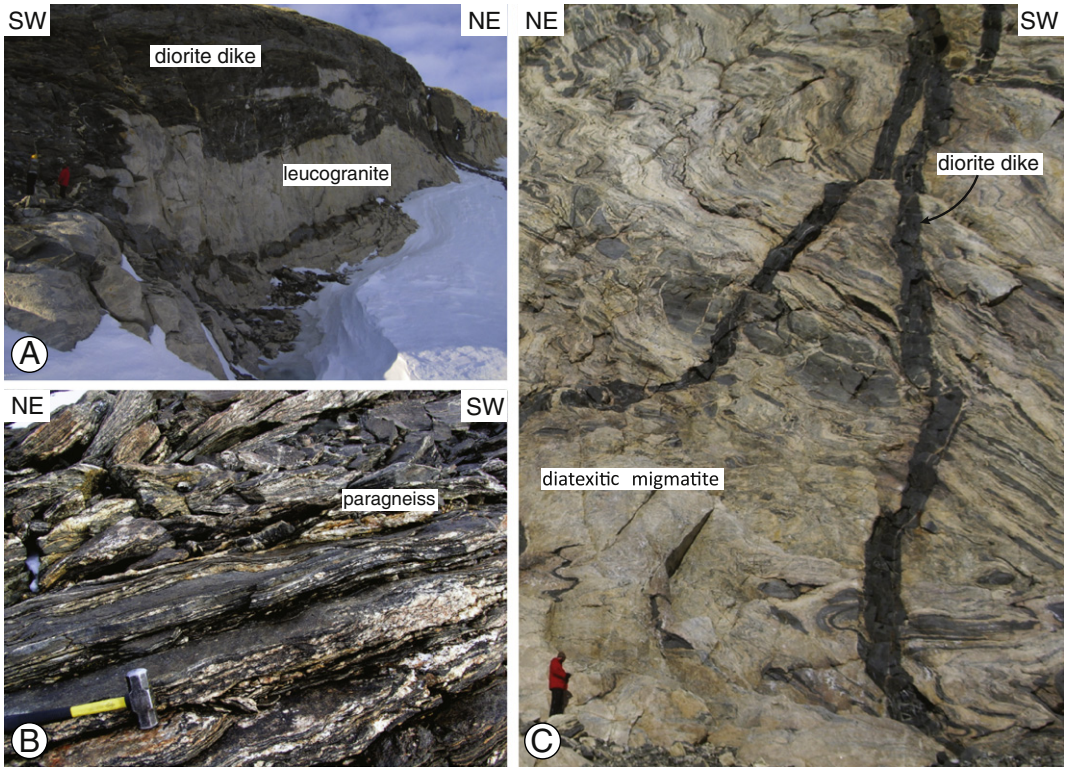

Fig. 3. Field photos of representative $^{40}Ar/^{39}Ar$ sample localities. (A) Diorite dike (M5-I7) on Mount Iphigene that cuts across compositional layering and foliation, but is folded and interdigitated with neighboring leucogranite: photo by S.C. Kruckenberg. (B) Paragneiss (M5-G174B) from within the South Fosdick Detachment zone on Mount Getz that shows strong foliation defined by biotite and asymmetric feldspar aggregates. (C) Folded migmatites and granites that are crosscut by folded diorite dikes (black) from Mount Ferranto. The diorite dikes have granitic xenoliths; their margins are irregular and are incorporated into the folded gneissic foliation. The diorite dikes have brittle fractures that are filled by leucogranitic material. Meter-scale dikes define disharmonic folds and indicate passive folding during flow of partially molten crust. The folded migmatites display the accumulation of granitic material (light yellow) along the synformal hinge zones of asymmetric folds and the accumulation of granitic material that dismembered residuum (migmatite portion that experienced melt loss) layers (gray). The residuum blocks are fractured and the fractures are filled by leucogranitic material.

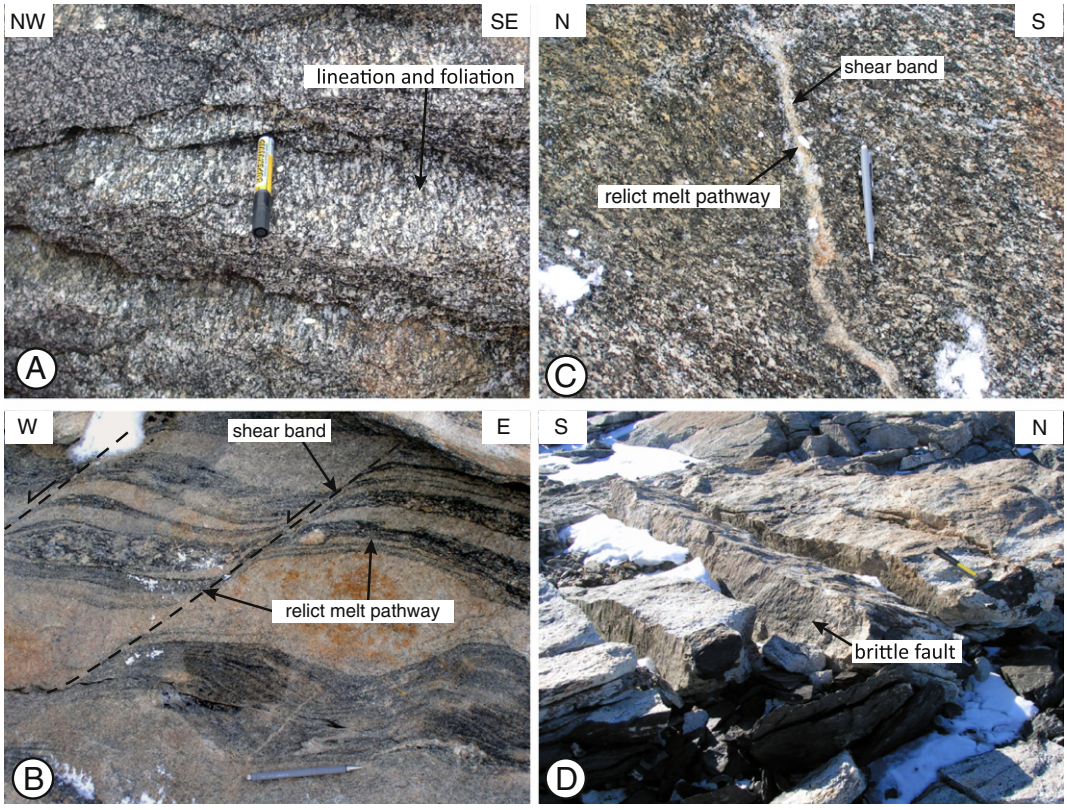

Fig. 4. Field photos of structures that display overprinting relationships within the South Fosdick Detachment zone on Mount Richardson. (A) Migmatitic biotite orthogneiss that displays a strong lineation and a moderate foliation. Lineation trend is 225°. (B) Migmatitic biotite orthogneiss and concordant leucogranite layers that display a strong foliation. Leucogranite layers and orthogneiss layers are boudinaged and offset by normal sense shear bands that indicate top-to-the-SW shear sense. Shear bands and concordant leucosomes represent relict melt pathways. (C) Shear band filled with granite that shows visible offset of the gneissic foliation. The shear band strikes 105°. The granite-filled shear band represents a relict melt pathway. (D) Brittle faults with a 095° strike that overprint high temperature fabrics. Faults contain slickensides consisting of chlorite and muscovite. Muscovite on brittle faults may indicate relict fluid pathways during final stages of granite crystallization.

granites were emplaced late in the development of the SFD zone between ca. 102 and 97 Ma (McFadden et al., 2010a,2010b; Yakymchuk et al., 2013a).

Crystallization ages for the structurally discordant granite dikes aid in bracketing deformation within the SFD zone. A non-foliated granitic dike that crosscuts the SFD zone solid-state fabric provides a lower age limit on deformation at ca. 97–96 Ma (McFadden et al., 2007, 2010b). A similar U–Pb age was obtained on monazite from a post-kinematic granite stock (Richard et al., 1994). U–Pb SHRIMP titanite ages for diorite dikes that crosscut the gneissic foliation range from ca. 101 to 97 Ma (McFadden et al., 2010b). A 99.7 ± 0.8 Ma deformed diorite dike and a 96.7 ± 0.9 Ma undeformed diorite dike indicate the dikes intruded during the latest movements of the SFD system (McFadden et al., 2010a). Dike emplacement coincided with, or narrowly preceded, the crystallization and cooling of the entire gneiss dome, as documented by $^{40}Ar/^{39}Ar$ cooling ages between ca. 101 and 94 Ma for hornblende, muscovite, biotite, and K-feldspar across the range (Richard et al., 1994). $^{40}Ar/^{39}Ar$ muscovite (neo-crystallization or cooling) ages on muscovite-bearing brittle shears are ca. 96 Ma (Richard, 1992; Richard et al., 1994).

4. Structures and kinematics within the Fosdick dome

Within the Fosdick Mountains, fabrics and structures are characterized relative to emplacement of the leucogranite sheets and movement along the SFD. These are: 1) "Early" syn-kinematic footwall/detachment fabrics and structures; 2) "Late" syn-kinematic footwall/detachment fabrics and structures; and 3) "Latest" post-kinematic hanging wall fabrics and structures.

4.1. "Early" syn-kinematic footwall/detachment fabrics and structures

The "early" stage fabrics and structures represent high temperature deformation that occurred in the presence of melt and magma. Penetrative foliation generally dips 20–30° to the S and steepens locally at Mount Richardson (Fig. 3B). Open and upright meter-scale corrugations fold the detachment shear zone foliation. Rocks in the shear zone are mostly L > S tectonites with lineation defined by stretched quartz, biotite, and sillimanite. L-tectonites occur near the domain of steeply dipping foliation on Mount Richardson (Fig. 4A). The dominant mineral stretching lineation is oriented 10°, 235° (Fig. 5A). An overprinting crenulation lineation, associated with the corrugations, is oriented 07°, 080° (McFadden et al., 2007). Asymmetric feldspar porphyroclasts and S–C structures display top-to-the-SW oblique motion (McFadden et al., 2007). Feldspar porphyroclasts commonly display internal microfracturing, whereas quartz grains display dynamic recrystallization and a strong crystallographic preferred orientation, indicating crystal-plastic deformation (McFadden et al., 2007). Sigmoidal boudins of orthogneiss and boudins of leucogranite also record top-to-the-SW shear sense (Fig. 4C).

Leucogranite sheets, associated with the leucogranite-sheeted complex in the footwall, intrude portions of the SFD. A tabular leucogranite body with margins that are interdigitated with the gneissic foliation and interfoliated with the migmatites indicates syntectonic emplacement into the SFD. Leucogranite dikes and veins connected with the tabular leucogranite are intercalated and deformed along with the paragneiss and orthogneiss layers (Fig. 4B) (McFadden et al., 2010b).

Granite-filled inter-boudin regions and extensional shear bands that occur within the footwall and the SFD shear zone represent relict melt pathways (Fig. 4B, C). Synthetic top-to-the-SW shear bands that

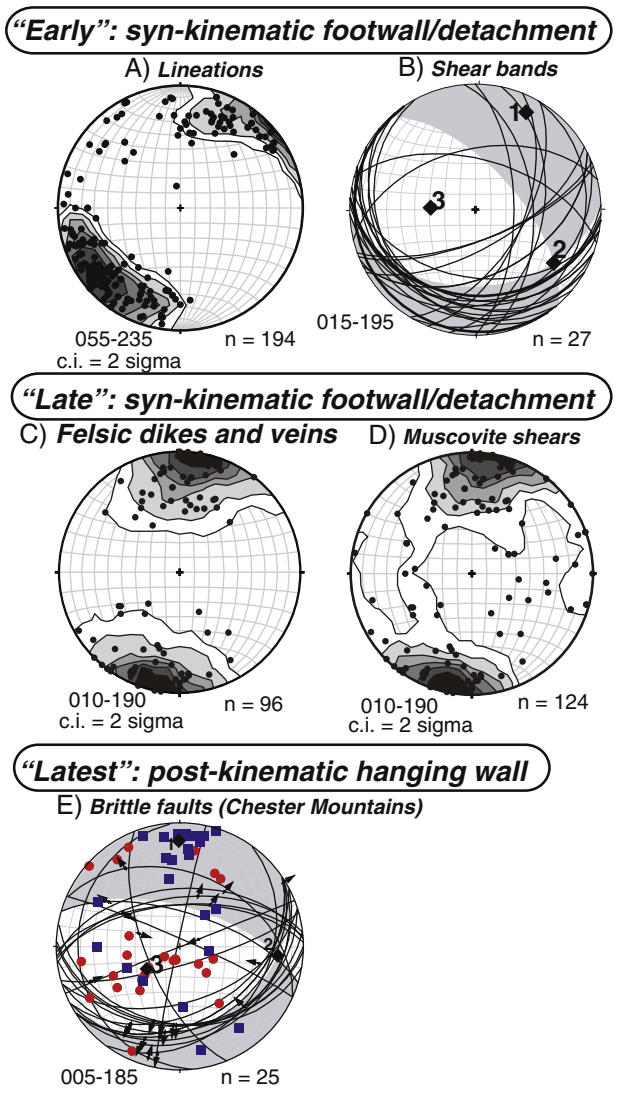

Fig. 5. Equal area projections display data points, kamb contours (2σ contour interval (c.i.)), and kinematic solutions from the Fosdick Mountains. A, B) These data display fabric data from syn-kinematic footwall and detachment rocks that represent the "early" stage in the emplacement and exhumation of the Fosdick dome: A) mineral stretching lineations; B) normal-sense extensional shear bands; numbers represent strain axes. C, D) These data display fabric data from syn-kinematic footwall and detachment rocks that represent the "late" stage in the emplacement and exhumation of the Fosdick dome: C) poles to N–S dipping felsic veins and dikes (from Richard, 1992); D) poles to N–S dipping muscovite shears from the SFD (from Richard, 1992). E) These data display brittle shears from the hanging wall in the Chester Mountains. The faults are the "latest" stage in the Fosdick dome exhumation history; numbers represent strain axes. Red circles represent maximum compression direction and blue squares represent maximum tension direction. Equal area projections were made with Stereonet v. 6.3.3 by R.W. Allmendinger. Kinematic solutions were calculated with the FaultKin 4.3.5 application, by R.W. Allmendinger.

crosscut the gneissic foliation are common and antithetic top-to-the-NE shear bands are rare. The extensional shear bands range from centimeter- to meter-scale, with widths ranging from 1 to 10 cm. Kinematic analysis of the shear bands defines a principal extension direction (T) of 13°, 028°, and a shortening direction (P) of 61°, 273° (Fig. 5B) (McFadden et al., 2007).

4.2. "Late" syn-kinematic footwall/detachment fabrics and structures

A conjugate array of moderately dipping brittle faults, felsic veins and dikes (aplites), mafic dikes, and muscovite-coated brittle fractures crosscut the "early" fabrics and structures. The overprinting relationships between these structures are found throughout the upper portions of the SFD footwall, but they are best exposed within the SFD shear zone at Mount Richardson. The mafic dikes, aplites, and the muscovite-coated brittle shears are nearly subvertical and strike ESE–WNW. These structures record stretching oriented 010°–190° (Fig. 5C, D) (Richard, 1992; Siddoway et al., 2004b, 2005). The mafic dikes have sharp planar contacts and are not foliated (Richard et al., 1994). The aplite dikes range in thickness from ~10 cm to 1 m and have sharp planar contacts with the migmatites. Stretched quartz and chloritic streaks define normal dip-slip to normal oblique-slip faults. Shear fracture analysis indicates (T) and (P) axes oriented 11°, 202°, and 72°, 331°, respectively (McFadden et al., 2007). The origin of the muscovite-coated shears has been enigmatic (cf. Richard et al., 1994), but likely they served as migration pathways for late stage fluids released upon the crystallization of voluminous migmatite and granite, as evidenced by the neocrystallization of muscovite and other hydrous phases.

4.3. "Latest" post-kinematic hanging wall fabrics and structures

In the Chester Mountains, which are inferred to expose a part of the hanging wall of the SFD, late- to post-kinematic minor brittle faults that strike ENE crosscut non-metamorphosed and massive Ford Granodiorite (Fig. 2). Kinematic analysis of the geometries and slip sense of brittle structures indicate the principal extension axes are oriented 19°, 003°, and the shortening axes are oriented 60°, 232° (McFadden et al., 2007). The ENE-striking faults have chloritic brittle shear surfaces that record normal oblique slip (Siddoway, 2008).

5. Thermochronology

Previous studies concluded that the Fosdick dome sustained high temperatures during detachment tectonics and then underwent rapid cooling (McFadden et al., 2010a; Richard et al., 1994; Siddoway et al., 2004b). This study confirms and refines this rapid cooling history from zircon crystallization through biotite closure temperature in the Fosdick dome.

5.1. Methods for $^{40}Ar/^{39}Ar$ geochronology

$^{40}Ar/^{39}Ar$ geochronology by infrared laser (CO_2) step heating of single and multiple grains was conducted at the U.S. Geological Survey in Denver, Colorado. Hornblende and biotite were purified to >99% by crushing, washing, magnetic separation, and handpicking. The mineral separates and the Fish Canyon Tuff sanidine standard (28.201 Ma; Kuiper et al., 2008) were irradiated for 20 MWH in the central thimble position of the U.S. Geological Survey Triga reactor in Denver, Colorado (Dalrymple et al., 1981). Samples were cadmium-lined to minimize ^{40}Ar production. All analyses were made by progressively heating single and multiple (up to 5) grains using a 25 W CO_2 laser equipped with a beam homogenizer with a custom designed and constructed ultra high vacuum extraction line, and isotopic ratios were measured by peak hopping with an electron multiplier in analog mode using a Mass Analyzer Products 215–50 mass spectrometer. Errors on all ages in the figures and tables are reported at the 2σ-confidence level. All measured isotopes and errors (1σ uncertainties) together with the $^{40}Ar/^{39}Ar$ ages and errors (2σ uncertainties) are given in Table DR1 and the data are plotted (with 2σ uncertainties) as age spectra (Figs. 6 and 7), assuming a present day $^{40}Ar/^{39}Ar$ value of 298.56 (Lee et al., 2006) and the decay constants of Min et al. (2000). Age plateaus were determined if two or more consecutive heating steps contained at least 50% of the ^{39}Ar released from the sample, and if radiogenic $^{40}Ar/^{39}Ar$ values for these heating steps overlap at the 95% confidence level.

Coexisting hornblende and biotite $^{40}Ar/^{39}Ar$ ages were determined from three syntectonic diorite dikes and sills to clarify the cooling history in the Fosdick dome and to assess the influence of the SFD on the cooling history. In addition, biotite $^{40}Ar/^{39}Ar$ cooling ages were

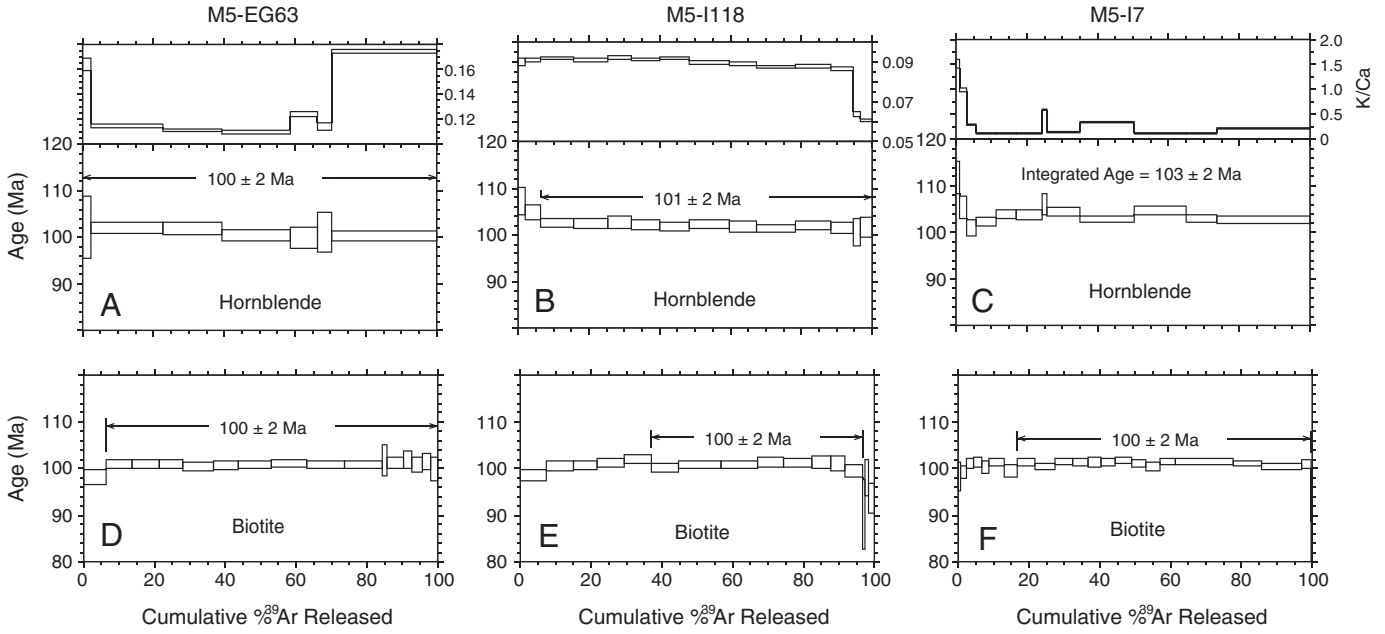

Fig. 6. Plots show $^{40}Ar/^{39}Ar$ age spectra from syntectonic diorite dikes and sills. (A) Hornblende $^{40}Ar/^{39}Ar$ age spectra for sample M5-EG63 from East Getz. Hornblende $^{40}Ar/^{39}Ar$ age spectra for (B) sample M5-I118 and (C) sample M5-I7 from Mount Iphigene. Errors on plotted release step ages and calculated ages are 2σ. Biotite $^{40}Ar/^{39}Ar$ age spectra for (D) sample M5-EG63, (E) M5-I118, and (F) M5-I7.

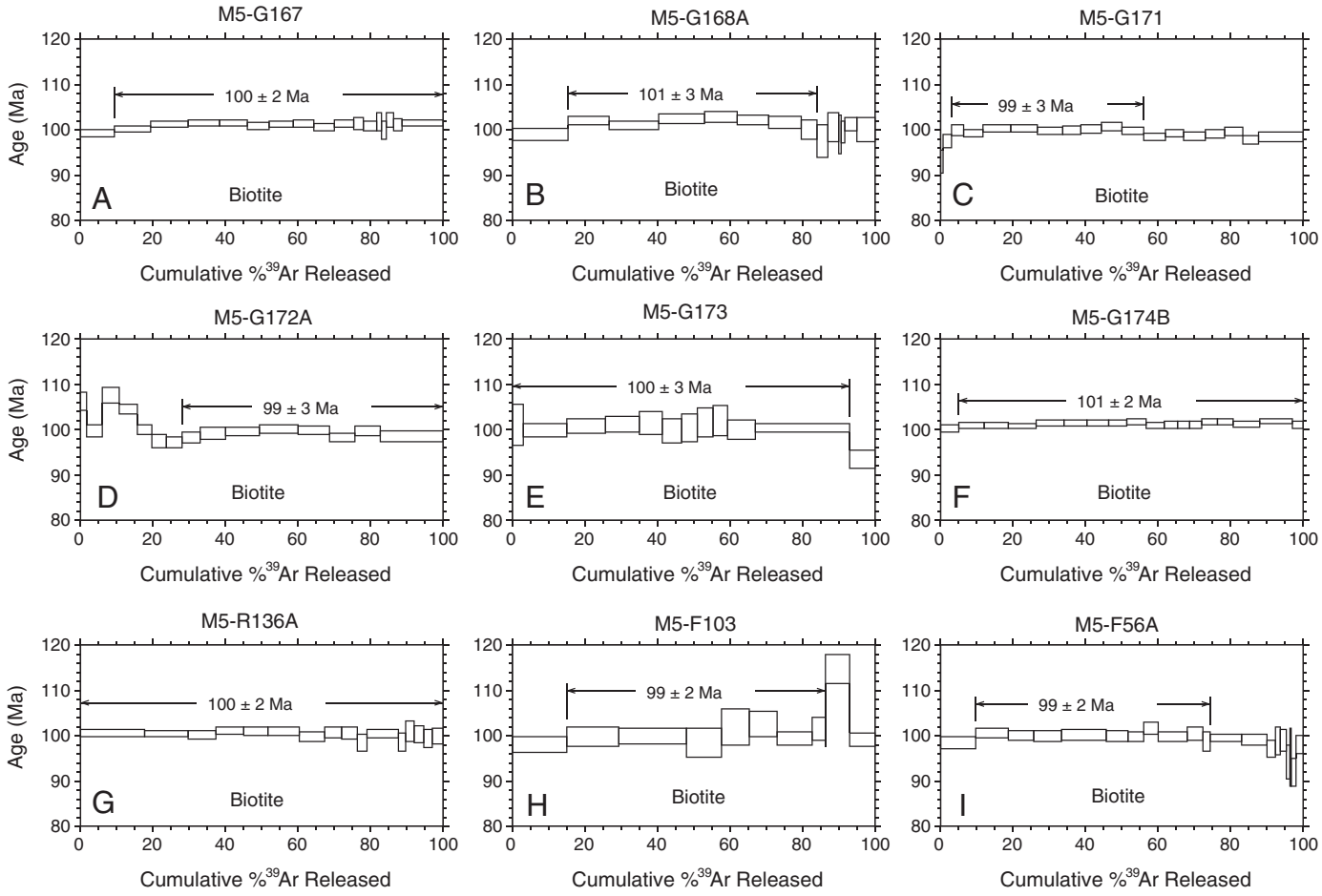

Fig. 7. Biotite $^{40}Ar/^{39}Ar$ age spectra for (A) sample M5-G167, (B) sample M5-168A, (C) sample M5-G171, (D) sample M5-G172A, (E) sample M5-G173, (F) and sample M5-G174B from a transect across the South Fosdick Detachment zone on Mount Getz. Biotite $^{40}Ar/^{39}Ar$ age spectra for (G) sample M5-R136A from Mount Richardson. Biotite $^{40}Ar/^{39}Ar$ age spectra for (H) sample M5-F103 and (I) sample M5-F56A from Mount Ferranto. Errors on plotted release step ages and calculated ages are 2σ.

determined from two migmatite localities within the footwall of the Fosdick dome and from seven migmatitic units that experienced solid-state deformation within the SFD. For all of the samples selected, biotite and hornblende (where present) define the metamorphic foliation. Detailed EPMA data for samples across the Fosdick Mountains show consistent mineral chemistry (Smith, 1992).

5.2. Results

5.2.1. Diorite dikes and sills

Representative syntectonic diorite dikes and sills that intrude the migmatites and granites throughout the Fosdick dome were sampled for $^{40}Ar/^{39}Ar$ geochronology. The samples include a 60 m-thick, medium-grained diorite sill (M5-EG63) from East Getz, a lineated diorite dike (M5-I118), and a medium-grained 50 m thick diorite dike (M5-I7) from Mount Iphigene (Fig. 3A).

Hornblende and biotite grains from the East Getz diorite sill (M5-EG63) yield flat $^{40}Ar/^{39}Ar$ release spectra with identical plateau ages of 100 ± 2 Ma and 100 ± 2 Ma, respectively (Fig. 6A, D). Hornblende and biotite from the Mount Iphigene lineated diorite dike (M5-I118) yield plateau ages of 101 ± 2 Ma for the hornblende and 100 ± 2 Ma for the biotite (Fig. 6B, E). The Mount Iphigene diorite dike (M5-I7) hornblende separate yields a slightly disturbed $^{40}Ar/^{39}Ar$ spectrum, and although no true $^{40}Ar/^{39}Ar$ plateau age could be calculated, the sample has an integrated age of 103 ± 2 Ma (Fig. 6C). The biotite separate from the same sample yields a $^{40}Ar/^{39}Ar$ plateau age of 100 ± 2 Ma (Fig. 6F) (Table 1).

5.2.2. Migmatites and granites

In an attempt to assess the relationship between cooling histories in the SFD and the footwall, migmatites were sampled from the SFD and the footwall of the Fosdick dome. Six samples were collected from an ~50 m transect perpendicular to the detachment on Mount Getz, consisting of five migmatitic paragneisses (M5-G167, -G168A, -G171, -G173, and -G174B) and one granitic gneiss (M5-G172A) (Fig. 3B). One sample was also collected from a migmatitic orthogneiss (M5-R136A) within the SFD on Mount Richardson. Two samples from the footwall of the Fosdick dome at Mount Ferranto include a migmatitic garnet biotite metadiorite (M5-F56A) and a diatexitic migmatite (M5-F103) (Fig. 3C).

Biotite defines the foliation in the Mount Getz migmatitic paragneiss within the SFD and biotite separates from the migmatitic paragneisses all yield flat $^{40}Ar/^{39}Ar$ release spectra and exhibit minor disturbance during the early heating steps. Calculated $^{40}Ar/^{39}Ar$ plateau ages for these samples include 50–100% of total ^{39}Ar released. $^{40}Ar/^{39}Ar$ ages of biotite separates are 100 ± 2 Ma (M5-G167), 101 ± 3 Ma (M5-G168A), 99 ± 3 Ma (M5-G171), 99 ± 3 Ma (M5-G172A), 100 ± 3 Ma (M5-G173), and 101 ± 2 Ma (M5-G174B) (Fig. 7A–F). These samples all yield remarkably similar cooling ages. The migmatitic orthogneiss (M5-R136A) from Mount Richardson within the SFD contains biotite that defines the foliation and biotite separate yields a remarkably flat $^{40}Ar/^{39}Ar$ release spectrum and the calculated plateau age includes 100% of total ^{39}Ar released; the $^{40}Ar/^{39}Ar$ age is 100 ± 2 Ma (Fig. 7G).

The two samples from within the footwall of the Fosdick dome have $^{40}Ar/^{39}Ar$ ages similar to the SFD samples. The biotite separate from the diatexitic migmatite of Mount Ferranto (M5-F103) yields a relatively flat $^{40}Ar/^{39}Ar$ release spectrum, with slightly larger errors for each step, due to the smaller signal sizes. The plateau age includes 85% of total ^{39}Ar released and the $^{40}Ar/^{39}Ar$ plateau age is 99 ± 2 Ma (Fig. 7H). The biotite separate from the migmatitic garnet biotite metadiorite (M5-F56A) of Mount Ferranto yields a $^{40}Ar/^{39}Ar$ plateau age of 99 ± 2 Ma (Fig. 7I) (Table 1).

6. Titanium-in-zircon thermometry

Titanium concentrations from zircon grains were obtained by SHRIMP II at the Research School or Earth Sciences of the Australian National University (RSES-ANU) using methods similar to Hiess et al. (2008). Previous U–Th–Pb analytical spots (McFadden et al., 2010a) were lightly polished and then the same area within the grains was analyzed. The Ti concentrations were used to calculate the crystallization temperatures for zircon assuming TiO_2-saturated conditions according to:

$$T(°C) = [(4800 \pm 86)/(5.711 \pm 0.072) - (\log(Ti\ ppm))] - 273$$

(Ferry and Watson, 2007; Watson et al., 2006). Temperature estimates have been calculated assuming a_{Ti} and $a_{SiO2} = 1$; this is reasonable owing to quartz saturation and the presence of rutile. The thermometer is calculated for 10 kbar and the uncertainty is 5 °C/kbar, making the temperature estimates using this thermometer reasonable.

Crystallization temperatures calculated for 10 Cretaceous zircons from the Mount Richardson granodioritic orthogneiss, M5-R136, range from 615 °C to 730 °C, with two outliers at ~900 °C (Table 2). The M5-R136 zircon grains range in age from ca. 109 to 105 Ma (McFadden et al., 2010b). The average $T_{crystallization}$ for 10 zircons used for U–Pb age determination is 665 ± 48 °C (1σ) (Fig. 8). Uncertainty

Table 1
$^{40}Ar/^{39}Ar$ data from the Fosdick Mountains migmatite-cored gneiss dome.

Sample	Rock type[a]	Latitude	Longitude	Peak	Mineral[a]	Age (Ma)[b]	Uncertainty[c]	%^{39}Ar[d]	MSWD	Comments
M5-EG63	hb bt diorite sill	S76° 32.633	W145° 02.778	East of Getz	Hb	100	2	100	1.49	
					Bt	100	2	95.2	0.36	
M5-I118	hb bt diorite dike	S76° 32.146	W145° 51.053	Mount Iphigene	Hb	101	2	93.5	0.79	
					Bt	100	2	59.6	1.3	
M5-I7	hb bt diorite sill	S76° 31.938	W145° 49.875	Mount Iphigene	Hb	103	2	–	3.1	integrated age
					Bt	100	2	83	1.2	
M5-G167	gt bt crd sil paragneiss	S76° 33.249	W145° 12.739	Mount Getz	Bt	100	2	90.5	1.2	
M5-G168A	gt bt crd sil paragneiss	S76° 33.222	W145° 12.190	Mount Getz	Bt	101	3	68.6	1.9	
M5-G171	gt bt crd sil paragneiss	S76° 33.117	W145° 12.038	Mount Getz	Bt	99	3	53	0.8	
M5-G172A	bt granitic gneiss	S76° 33.159	W145° 11.950	Mount Getz	Bt	99	3	71.9	2.1	
M5-G173	gt bt crd sil paragneiss	S76° 33.216	W145° 12.068	Mount Getz	Bt	100	3	93.2	0.4	
M5-G174B	gt bt crd sil paragneiss	S76° 33.237	W145° 12.055	Mount Getz	Bt	101	2	94.8	1.1	
M5-R136A	migmatitic bt orthogneiss	S76° 32.877	W144° 41.247	Mount Richardson	Bt	100	2	100	1.2	
M5-F103	diatexitic bt migmatite	S76° 29.258	W145° 32.654	Mount Ferranto	Bt	99	2	71.5	1.2	
M5-F56A	gt bt paragneiss	S76° 29.744	W145° 32.055	Mount Ferranto	Bt	99	2	64.6	1	

Note: MSWD–mean square of weighted deviates for plateau age.
[a] Mineral abbreviations: bt—biotite, hb—hornblende, gt—garnet, crd—cordierite, sil—sillimanite.
[b] Weighted plateau ages unless otherwise noted in comments.
[c] 2σ uncertainty.
[d] %^{39}Ar—percentage of ^{39}Ar used in weighted plateau age calculation.

Table 2
Ti concentrations and temperature estimates from the Fosdick gneiss dome.

Spot	Ti ppm	±2σ	T (°C) zircon	U–Pb age (Ma)	±2σ
R136A-17.1	2.025	0.62	615	105.4	1.2
R136A-17.2	11.026	2.04	755	105.7	1.2
R136A-1.1	2.381	0.75	627	108.9	1.1
R136A-1.2	4.558	0.65	677	110.9	1.2
R136A-15.1	2.277	0.82	624	102.1	1.1
R136A-2.1	33.754	2.57	875	108.7	1.1
R136B-1.1	42.763	3.21	903	104.6	1.1
R136B-2.1	8.108	1.59	727	111.5	1.2
R136B-14.1	3.135	0.72	647	106.5	1.5
R136B-6.1	5.440	1.16	692	109.6	1.4

Temperature estimates have been calculated with equations form Ferry and Watson (2007) assuming an $a_{SiO2} = 1$ and $a_{TiO2} = 1$.

linked to calculating $T_{crystallization}$ with Ti-in-zircon thermometer has been estimated by Ferry and Watson (2007) at 8 °C (2σ). There is no apparent correlation between Ti concentration and U–Pb age (Fig. 8B).

7. Discussion

7.1. Cooling of the Fosdick dome

In the Fosdick Mountains, temperature (T)–time (t) paths interpreted from combined geochronologic data indicate that the youngest suite of voluminous migmatites and granites crystallized between ca. 109 and 102 Ma and underwent rapid cooling between ca. 102 and 95 Ma (Fig. 9). Rapid cooling proceeded from granite crystallization through biotite closure temperature from ca. 102 to 99 Ma followed by slower cooling from biotite closure temperature through K-feldspar

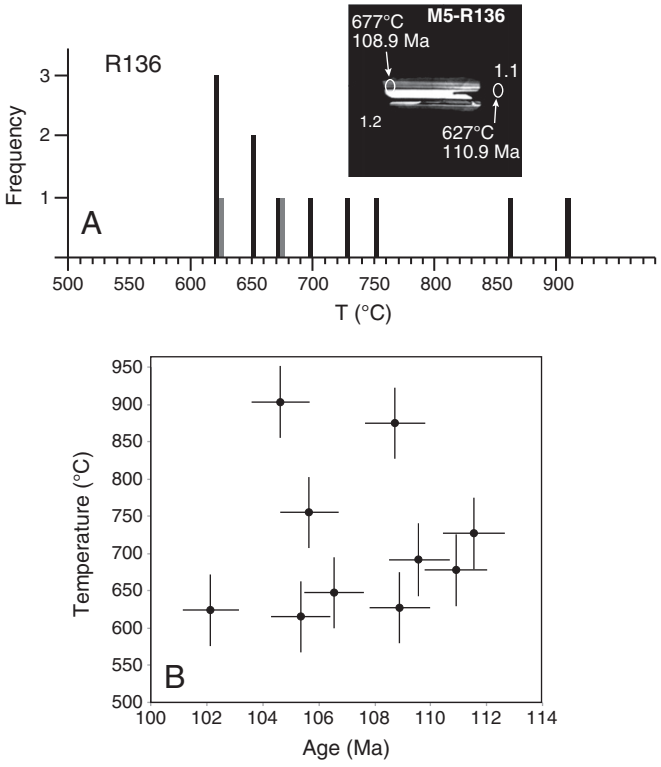

Fig. 8. (A) Histogram showing the temperature distribution from Ti-in-zircon thermometry for sample M5-R136. Inset shows a cathodoluminescence image of an oscillatory-zoned zircon grain with a dark rim. The spots labeled on the zircon grain are where the Ti concentration analyses were taken after U–Pb zircon analyses were completed using the SHRIMP II. (B) Plot of variation of temperature obtained by Ti-in-zircon thermometry vs. U–Pb age of zircons from the Fosdick dome. Crystallization temperatures do not define a clear trend with age. Vertical error bars represent uncertainty in temperature from Ti-in-zircon thermometry and horizontal error bars represent uncertainty in U–Pb ages.

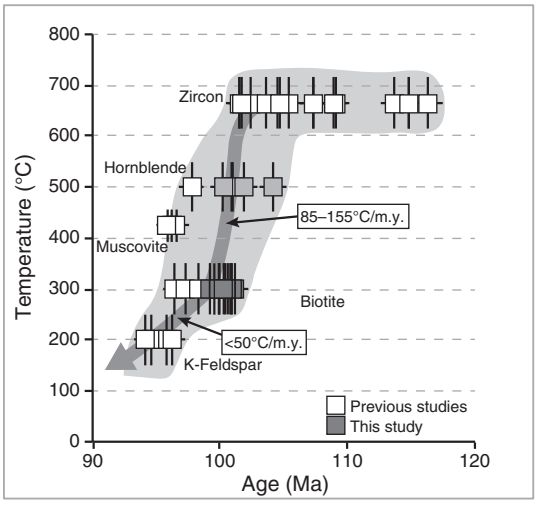

Fig. 9. (A) Temperature (T)–time (t) diagram for U–Pb and $^{40}Ar/^{39}Ar$ data from the Fosdick Mountains. Zircon crystallization temperature is based on titanium-in-zircon analyses. Vertical bars represent uncertainties in closure temperature or crystallization temperature and horizontal bars represent uncertainty of age determinations. The previous data presented in this figure are fromRichard et al. (1994), McFadden et al. (2007, 2010a, 2010b), Korhonen et al. (2010b), and Yakymchuk et al. (2013a).

closure temperature from ca. 99 to 95 Ma. Cooling ages within the Fosdick dome are significantly younger than cooling ages to the N of the dome. North of the Balchen Glacier fault, granodiorite at Lewis Rocks within the Phillips Range has biotite $^{40}Ar/^{39}Ar$ cooling ages of 355.9 ± 1.0 Ma and muscovite $^{40}Ar/^{39}Ar$ cooling ages of 345.9 ± 0.7 Ma (Fig. 2) (Richard et al., 1994). Granodiorite in the Chester Mountains, to the S of the SFD, has slightly older Cretaceous biotite and K-feldspar $^{40}Ar/^{39}Ar$ cooling ages of 105.2 ± 0.3 Ma and 101.0 ± 2.4 Ma, respectively (Fig. 2). These relationships emphasize that the Fosdick dome contains rocks that show the youngest cooling ages in the region and that it is bounded by crustal-scale faults. It is possible that the granodiorite with Paleozoic $^{40}Ar/^{39}Ar$ ages represents the hanging wall of the detachment system that exhumed the Cretaceous migmatites, if the amount of lateral translation on the Balchen Glacier fault (which is unconstrained) has been small.

For the following discussion we used closure temperature estimates of 500 ± 50 °C for hornblende (McDougall and Harrison, 1999), 425 ± 25 °C for white mica (Harrison et al., 2009), 300 ± 50 °C for biotite (Harrison et al., 1985), and 200 ± 50 °C for K-feldspar (Lovera et al., 1989). The closure temperature estimates may be affected by cooling rate, mineral composition, and grain size (Harrison et al., 1985; Hess et al., 1993). During rapid cooling (>100 °C/Ma) the nominal argon closure temperatures of hornblende (Ar closure ~ 550 °C) and biotite (Ar closure ~ 300 °C) can be significantly higher than generally assumed (e.g. Villa, 1998). In addition, the cooling rates are calculated using U–Pb and Ar/Ar ages that are close in age. These similar ages can produce high cooling rates because the errors on decay constants for the two systems are different (e.g. Willigers et al., 2001). However, we suggest that the close proximity of ages and rapid cooling rates display significant tectonic events, such as detachment initiation and footwall rock exhumation.

The high to moderate temperature cooling in the Fosdick dome, from granite crystallization through biotite closure temperature, was rapid. Ti-in-zircon data indicate at ca. 102 Ma the minimum granite crystallization temperatures were ~665 ± 48 °C, down from peak temperatures of ~850 °C attained during anatexis (determined from mineral equilibrium modeling;Korhonen et al., 2010a). The nearly identical biotite and hornblende cooling ages with flat $^{40}Ar/^{39}Ar$ spectra are consistent with rapid cooling of the dome. On the basis of these cooling ages and the crystallization temperature of the granites, the cooling rate in the Fosdick dome through the biotite closure temperature was 85 to

155 °C/m.y. (Fig. 9). The cooling rate appears to decrease dramatically to a maximum of 50 °C/m.y. from biotite through K-feldspar closure temperatures. Alternatively, a more conservative estimate of cooling rate for the Fosdick dome from granite crystallization through K-feldspar closure would range from 50 to 80 °C/m.y. The cooling ages from muscovite grains were not used to determine cooling rates because muscovite is not a pervasive equilibrium phase; it is localized on late brittle shear surfaces (Richard et al., 1994), arising from release of late fluids during final crystallization and cooling of the dome granites and migmatites. It is likely that the muscovite $^{40}Ar/^{39}Ar$ ages from brittle shears represent neo-crystallization ages that formed below the closure temperature of muscovite.

The Fosdick dome preserves evidence for near-isothermal decompression and rapid cooling at high to moderate temperatures. During the initial stages of exhumation of the Fosdick dome, cordierite-bearing assemblages and textures indicate near-isothermal decompression (Siddoway et al., 2004b). Temperature during decompression probably remained constant owing to the combined effect of heat advection and heat input from intrusive leucogranite sheets (e.g. Langille et al., 2012). Continued emplacement of leucogranite in a region of compressed isotherms maintained very high heat flow to shallow depths, resulting in extremely rapid cooling when the system was finally exhumed. Emplacement of the leucogranite sheets may have localized the detachment zone at the interface of very hot crust and brittle crust, which initiated the SFD system (McFadden et al., 2010a).

7.2. Kinematic evolution of the Fosdick dome

The “early” and “late” syn-kinematic footwall/detachment fabrics and structures highlight the abrupt transition from exhumation to emplacement and cooling of the Fosdick dome. Melt- and magma-related structures associated with voluminous leucogranite sheets were overprinted by solid-state deformation, defined as the SFD zone, and crosscutting brittle structures transported late silicate melt and fluids during cooling of the Fosdick dome (McFadden et al., 2010a; Richard, 1992).

The “early” syn-kinematic fabrics and structures record significant deformation in the presence of melt. Leucogranite sheets, granite dikes and veins, granite-filled inter-boudin regions and shear bands, and leucosomes show the presence of former melt and relict melt pathways. Solid-state deformation within the SFD zone overprinted many of these structures. Leucogranite sheets, granite dikes, and granite-filled shear bands also intruded the solid-state deforming SFD zone (Fig. 4B, C). This suggests that the transport of crustally derived melt and granite crystallization was still occurring during the progression of the SFD system. Stretching lineations within the “early” syn-kinematic domain, oriented 055°–235°, record oblique extensional deformation, and S–C fabrics and asymmetric porphyroclasts record top-to-the-SW oblique motion (Fig. 5A). Exhumation associated with the SFD ultimately caused the cessation of melt transfer and culmination of granite crystallization within the Fosdick dome.

The “late” syn-kinematic fabrics and structures that transect the “early” syn-kinematic fabrics and structures record a distinct change in the maximum stretching direction within the SFD system. The “late” syn-kinematic structures, including brittle faults, mafic dikes, muscovite shears, and aplite veins and dikes indicate maximum stretching oriented 010°–190° (Fig. 5C, D) (Richard, 1992; Richard et al., 1994), whereas fabrics in the “early” domain indicate maximum stretching oriented 055°–235°.

The significant change in maximum stretching direction could be related to large-scale tectonic plate movements or could be due to changes in the local strain field. Dextral translation commenced along the East Gondwana margin from ca. 128 Ma (Jacob and Dyment, 2014), owing in part to oblique subduction (Sutherland and Hollis, 2001). Between ca. 107 and 103 Ma, a significant change in the strain field was recorded on the Antarctic Peninsula, based on structural and thermochronologic data (Vaughan et al., 2012). The timing of this tectonic reorganization aligns temporally with the transition from wrench to oblique extension recorded in the crustally derived granites of the Fosdick Mountains (McFadden et al., 2010a, 2010b; Yakymchuk et al., 2013a), and in 070°–250°-directed opening of mafic dikes and brittle faults outside the Fosdick dome, in the Ford Ranges (Siddoway, 2008; Siddoway et al., 2005). In the Fosdick Mountains, an additional transition in the strain field occurred between ca. 102 and 96 Ma, based on an U–Pb zircon age of ca. 102 Ma in the “early” structures (McFadden et al., 2010a) and $^{40}Ar/^{39}Ar$ muscovite ages of ca. 96 Ma (Richard et al., 1994) in the “late” structures. The “early” to “late” syn-kinematic structures that formed in response to a change in maximum stretching direction, and the rapid cooling, appear to be specific to the Fosdick Mountains dome, and therefore probably are not due to far-field tectonic processes.

The presence of aplite dikes and veins and muscovite-coated shears may be due to rapid cooling and granite crystallization causing a negative volume change that induced fractures and tensile openings according to the ambient stress within the footwall. The openings served as pathways for silicate melts and late fluids now represented by aplites and muscovite-coated shear surfaces (e.g. Druguet et al., 2008; Karlstrom et al., 1993). For this reason, the muscovite within late crosscutting structures has $^{40}Ar/^{39}Ar$ ages younger than the biotite cooling ages from gneisses. The “latest” post-kinematic structures, represented by hanging wall brittle faults exposed in the Chester Mountains and Neptune Nunataks, record similar stretching oriented 005°–185° (McFadden et al., 2007), indicating that brittle deformation of the hanging wall occurred in response to southward translation relative to the exhuming Fosdick dome rocks.

7.3. Rapid cooling in gneiss domes and MCCs

In the footwall and detachment units of MCCs, the proximity in age of granite and/or migmatite crystallization and moderate temperature thermochronometers (<300 °C), as well as the presence of textures associated with near-isothermal decompression, indicate exhumation of hot, deep crustal rocks followed by shallow emplacement and rapid cooling, which are characteristic for migmatite-cored gneiss domes and MCCs (e.g. Whitney et al., 2013, for a review). Here, the hot rocks are close enough to the surface that heat advection is no longer a viable mechanism for cooling (e.g. Whitney et al., 2013). Instead, cooling occurs by conduction of heat to the Earth's surface (e.g. Foster et al., 1992). The northern North American Cordillera MCCs record near-isothermal decompression (Norlander et al., 2002; Kruckenberg and Whitney, 2011; Goergen and Whitney, 2012) and cooling through argon thermochronometers within 5 to 10 m.y. (Fayon et al., 2004; Foster et al., 2001; Gordon et al., 2008; Kruckenberg et al., 2008; Norlander et al., 2002). Low-temperature thermochronologic data, such as fission-track and U/Th–He apatite ages, show that the migmatites and leucogranites within the Thor-Odin dome (British Columbia, Canada) reached the near surface (<2 km depth) shortly after cooling through the closure temperature of micas, highlighting extreme short-lived geothermal gradients that are preserved in MCCs (Toraman et al., 2014). Finally, heat could also be removed by the convective circulation of surface water in the hanging wall of the detachments (e.g., Gottardi et al., 2011).

In the Liaodong Peninsula MCCs in China, U–Pb ages and cooling ages through K-feldspar closure are within 10–15 m.y., indicating cooling rates range from 30 to 55 °C (Charles et al., 2012; Lin et al., 2008; Wu et al., 2005; Yang et al., 2007). Aegean MCCs preserve a transition within 2–4 m.y. from migmatite/granite crystallization through low T mineral closure (Brichau et al., 2008; Keay et al., 2001). Shallow emplacement of migmatite is a feature of “fast extension” models for MCCs, where, during isothermal decompression, partially molten rocks are advected to the very shallow crust (~5 km) before melt crystallizes (Rey et al., 2009a,2009b). Models also show that the presence of a low viscosity crust enhances the localization of detachments and

the formation of rolling-hinge detachment systems that are very efficient at exhuming large volumes of hot crust (Lavier and Buck, 2002; Whitney et al., 2013).

In the Fosdick Mountains the Cretaceous migmatite core records high metamorphic temperatures (>800 °C) at relatively shallow depths (<7.5 kbar), indicating that the crust was not significantly thickened. Possible evidence that heat was provided by magmatic underplating comes from isotopic characteristics of the Cretaceous mafic dikes (Saito et al., 2013). The partially molten crust registered near-isothermal decompression followed by rapid cooling through argon thermochronologic systems, tapering off in the final cooling stages. The crust at the surface today must have been very close to the surface in Cretaceous time, and any intervening crust was likely eroded since the inception of glaciations in Antarctica.

The mode of emplacement of the Fosdick Mountains migmatite was upward flow into an extensional opening in the Cretaceous upper crust, for example a pull-apart zone between strike–slip faults. The Balchen Glacier fault (Fig. 2) possibly represents one of these faults. Upward flow must have been allowed by lateral flow of the partially molten crust beyond the Fosdick Mountains dome, feeding the dome with low-viscosity, partially molten crust and plutonic bodies, as has been recently proposed for the Variscan Montagne Noire dome in the French Massif Central (Roger et al., 2015). In the Fosdick Mountains, much of the exhumation was accommodated by oblique extension on the SFD between 102 and 99 Ma. Rocks in both this detachment zone and its footwall cooled rapidly, such that they became part of the brittle crust. At this point, brittle fractures allowed pervasive fluid flow in the upper crust until ~96 Ma.

8. Summary

U–Pb zircon crystallization ages and $^{40}Ar/^{39}Ar$ hornblende and biotite cooling ages, over the time interval ca. 102–99 Ma, indicate cooling rates ranging from 85 to 155 °C/m.y. Rapid cooling followed a period of near-isothermal decompression and detachment tectonics that brought hot, deep migmatites and granites toward the surface. These migmatites and crustally-derived granites were emplaced at shallow levels in the crust, which led to rapid cooling owing to conductive heat loss. Below the biotite closure temperature (<300 °C) the cooling rate slowed. Near-isothermal decompression followed by rapid cooling is consistent with studies of numerous migmatite-cored gneiss domes and MCCs.

The “early” and “late” syn-kinematic fabrics and structures in the footwall and the detachment of the Fosdick dome represent the transition from exhumation and migmatite emplacement to localized nearly orthogonal extension during rapid cooling. The “early” syn-kinematic structures, including granite-filled inter-boudin regions and shear bands, and pervasive stretching lineation and gneissic foliation, characterize the emplacement phase of the Fosdick dome. The “late” syn-kinematic structures, such as the aplites and muscovite-coated shear surfaces denote localized nearly orthogonal extension. From the “early” to “late” structures the maximum stretching axis rotated in response to a local change in the strain field that may be due to extensional opening within a dilatant zone (releasing bend or megaboudin partition).

Acknowledgments

Research was funded by the National Science Foundation Office of Polar Programs grants NSF-OPP 0337488 to C. Teyssier and NSF-OPP 0338279 to C.S. Siddoway. We thank Mike Roberts, Forrest McCarthy, and Allen O'Bannon for field coordination and safety. For logistical support, we thank employees of Raytheon Polar Services, ANG 109th, and Kenn Borek Air crews. Reviews by B. Reno and N. Charles greatly improved the quality of this manuscript. Any use of trade, product, or firm names is for descriptive purposes only and does not imply endorsement by the U.S. Government.

Appendix A. Supplementary data

Supplementary data to this article can be found online at http://dx.doi.org/10.1016/j.lithos.2015.07.005.

References

Bradshaw, J.D., Andrew, B., & Field, B.D., 1983. Swanson Formation and related rocks of Marie Byrd Land and a comparison with the Robertson Bay Group of northern Victoria Land. In: Oliver, R.L., et al. (Eds.), Antarctic Earth Science: Australian Academy of Science. Canberra, pp. 274–279.

Bradshaw, J.D., Pankhurst, R.J., Weaver, S.D., Storey, B.C., Muir, R.J., & Ireland, T.R., 1997. New Zealand superterranes recognized in Marie Byrd Land and Thurston Island. In: Ricci, C.A. (Ed.), The Antarctic Region, Geological Evolution and Processes. Terra Antarctica Publication, Sienna, Italy.

Brichau, S., Ring, U., Carter, A., Bolhar, R., Monie, P., Stockli, D., & Brunel, M., 2008. Timing slip rate, displacement and cooling history of the Mykonos detachment footwall, Cyclades, Greece, and implications for the opening of the Aegean Sea basin. Journal of the Geological Society of London 165, 263–277.

Charles, N., Gumiaux, C., Augier, R., Chen, Y., Faure, M., Lin, W., & Zhu, R., 2012. Metamorphic core complex dynamics and structural development: field evidences from the Liaodong Peninsula (China, East Asia). Tectonophysics 560–561, 22–50. http://dx.doi.org/10.1016/j.tecto.2012.06.019.

Coney, P.J., & Harms, T.A., 1984. Cordilleran metamorphic core complexes: Cenozoic extensional relics of Mesozoic compression. Geology 12, 550–554.

Crittenden, M.D.J., Coney, P.J., & Davis, G.H., 1980. Cordilleran Metamorphic Core Complexes (490 pp.).

Dalrymple, G.B., Alexander, E.C., Lanphere, M.A., & Kraker, G.P., 1981. Irradiation of samples for $^{40}Ar/^{39}Ar$ dating using the Geological Survey TRIGA reactor. U.S. Geological Survey Professional Paper 1176 (55 pp.).

Davey, F.J., & Brancolini, G., 1995. The Late Mesozoic and Cenozoic structural setting of the Ross Sea region. In: Cooper, A.K., Barker, P.F., Brancolini, G. (Eds.), Geology and Seismic Stratigraphy of the Antarctic MarginAntarctic Research Series 68. AGU, pp. 167–182.

Denele, Y., Lecomte, E., Jolivet, L., Lacombe, O., Labrousse, L., Huet, B., & Le Pourhiet, L., 2011. Granite intrusion in a metamorphic core complex: the example of the Mykonos laccolith (Cyclades, Greece). Tectonophysics 501, 52–70.

Druguet, E., Czeck, D.M., Carreras, J., & Castano, L.M., 2008. Emplacement and deformation features of syntectonic leucocratic veins from Rainy Lake zone (Western Superior Province, Canada). Precambrian Research 163, 384–400.

Fayon, A.K., Whitney, D.L., & Teyssier, C., 2004. Exhumation of orogenic crust: diapiric ascent versus low-angle normal faulting. In: Whitney, D.L., Teyssier, C., Siddoway, C.S. (Eds.), Gneiss Domes in Orogeny. Geological Society of America Special Paper 380, pp. 129–139.

Ferraccioli, F., Bozzo, E., & Damaske, D., 2002. Aeromagnetic signatures over western Marie Byrd Land provide insight into magmatic arc basement, mafic magmatism and structure of the eastern Ross Sea rift flank. Tectonophysics 347, 139–165.

Ferry, J., & Watson, E., 2007. New thermodynamic models and revised calibrations for the Ti-in-zircon and Zr-in-rutile thermometers. Contributions to Mineralogy and Petrology 154, 429–437.

Fitzgerald, P.G., & Baldwin, S.L., 1997. Detachment fault model for the evolution of the Ross embayment. In: Ricci, C.A. (Ed.), The Antarctic Region: geological evolution and processesTerra Antarctica Publication. Siena, Italy, pp. 555–564.

Flowers, R.M., Bowring, S.A., Tulloch, A.J., & Klepeis, K.A., 2005. Temperature of burial and exhumation within the deep roots of a magmatic arc, Fiordland, New Zealand. Geology 33, 17–20 (10/1130/G211010.1).

Forster, M.A., & Lister, G.S., 2003. Cretaceous metamorphic core complexes in the Otago Schist, New Zealand. Australian Journal of Earth Sciences 50, 181–198.

Foster, D.A., Harrison, T.M., Miller, C.F., & Howard, K.A., 1990. The $^{40}Ar/^{39}Ar$ thermochronology of the eastern Mojave Desert, California, and adjacent western Arizona with implications for the evolution of metamorphic core complexes. Journal of Geophysical Research 95, 20005–20024.

Foster, D.A., Miller, C.F., Harrison, T.M., & Hoisch, T.D., 1992. $^{40}Ar/^{39}Ar$ thermochronology and thermobarometry of metamorphism, plutonism, and tectonic denudation in the Old Woman Mountains area, California. Geological Society of America Bulletin 104, 176–191. http://dx.doi.org/10.1130/0016-7606.

Foster, D.A., Schafer, C., Fanning, C.M., & Hyndman, D.W., 2001. Relationships between crustal partial melting, plutonism, orogeny, and exhumation: Idaho–Bitterroot batholith. Tectonophysics 342, 313–350.

Gibson, G.M., McDougall, I., & Ireland, T.R., 1988. Age constraints on metamorphism and the development of a metamorphic core complex in Fiordland, southern New Zealand. Geology 16, 405–408.

Goergen, E.T., & Whitney, D.L., 2012. Corona networks as three-dimensional records of transport scale and pathways during metamorphism. Geology 40, 183–186.

Gordon, S.M., Whitney, D.L., Teyssier, C., Grove, M., & Dunlap, W.J., 2008. Timescales of migmatization, melt crystallization, and cooling in a Cordilleran gneiss dome: Valhalla complex, southeastern British Columbia. Tectonics 27. http://dx.doi.org/10.1029/2007TC002103.

Gottardi, R., Teyssier, C., Mulch, A., Vennemann, T.W., & Wells, M.L., 2011. Preservation of an extreme transient geotherm in the Raft River detachment shear zone. Geology 39, 759–762.
Harrison, T.M., Duncan, I., & McDougall, I., 1985. Diffusion of ^{40}Ar in biotite: temperature, pressure and compositional effects. Geochimica et Cosmochimica Acta 50, 2461–2468.
Harrison, T.M., Celerier, J., Aikman, A.B., Hermann, J., & Heizler, M.T., 2009. Diffusion of ^{40}Ar in muscovite. Geochimica et Cosmichimica Acta 73, 1039–1051 (10.1016/j.gca.2008.09.038).
Hess, J.C., Lippolt, H.J., Gurbanov, A.G., & Michalski, I., 1993. The cooling history of the late Pliocene Eldzhurtinskiy granite (Caucasus, Russia) and the thermochronological potential of grain-size age relationships. Earth and Planetary Science Letters 117, 393–406.
Hiess, J., Nutman, A.P., Bennet, V.C., & Holden, P., 2008. Ti-in-zircon thermometry applied to contrasting Archean metamorphic and igneous systems. Chemical Geology 247, 323–338.
Hollis, J.A., Clarke, G.L., Klepeis, K.A., Daczko, N.R., & Ireland, T.R., 2004. The regional significance of Cretaceous magmatism and metamorphism in Fiordland, New Zealand, from U–Pb zircon geochronology. Journal of Metamorphic Geology 22, 607–627.
Ireland, T.R., & Gibson, G.M., 1998. SHRIMP monazite and zircon geochronology of high-grade metamorphism in New Zealand. Journal of Metamorphic Geology 16, 149–167.
Jacob, J., & Dyment, J., 2014. Early opening of Australia and Antarctica: new inferences and regional consequences. Tectonophysics 636, 244–256.
Karlstrom, K.E., Miller, C.F., Kingsbury, J.A., & Wooden, J.L., 1993. Pluton emplacement along an active ductile thrust zone, Piute Mountains, southeastern California: interaction between deformational and solidification processes. Geological Society of America Bulletin 105, 213–230. http://dx.doi.org/10.1130/0016-7606.
Keay, S., Lister, G., & Buick, I., 2001. The timing of partial melting, Barrovian metamorphism and granite intrusion in the Naxos metamorphic core complex, Cyclades, Aegean Sea, Greece. Tectonophysics 342, 275–312.
Kimbrough, D.L., & Tulloch, A.J., 1989. Early Cretaceous age of orthogneiss from Charleston Metamorphic Group, New Zealand. Earth and Planetary Science Letters 95, 130–140. http://dx.doi.org/10.1016/0012-821X(89)90172-6.
Korhonen, F.J., Brown, M., Saito, S., & Siddoway, C.S., 2010a. Modeling multiple melt loss events in the evolution of an active continental margin. Lithos 116, 230–248. http://dx.doi.org/10.1016/j.lithos.2009.09.004.
Korhonen, F.J., Saito, S., Brown, M., Siddoway, C.S., & Day, J.M.D., 2010b. Multiple generations of granite in the Fosdick Mountains, Marie Byrd Land, West Antarctica: implications for polyphase intracrustal differentiation in a continental margin setting. Journal of Petrology 51, 627–670. http://dx.doi.org/10.1093/petrology/egp093.
Korhonen, F.J., Brown, M., Grove, M., Siddoway, C.S., Baxter, E.F., & Inglis, J.D., 2011. Separating metamorphic events in the Fosdick migmatite–granite complex, West Antarctica. Journal of Metamorphic Petrology 165–192.
Kruckenberg, S.C., & Whitney, D.L., 2011. Metamorphic evolution of sapphirine-bearing orthoamphibole-cordierite gneiss, Okanogan dome, Washington, USA. Journal of Metamorphic Geology 29, 429–449. http://dx.doi.org/10.1111/j/1525-1314.2010.00926.x.
Kruckenberg, S.C., Whitney, D.L., Teyssier, C., Fanning, C.M., & Dunlap, W.J., 2008. Paleocene-Eocene migmatite crystallization, extension, and exhumation in the hinterland of the northern Cordillera: Okanogan dome, Washington, USA. Geological Society of America 120, 912–929. http://dx.doi.org/10.1130/B26153.1.
Kuiper, K.F., Deino, A., Hilgen, F.J., Krijgsman, W., Renne, P.R., & Wijbrans, J.R., 2008. Synchronizing rock clocks of earth history. Science 320, 500–504. http://dx.doi.org/10.1126/science.1154339.
Langille, J.M., Jessup, M.J., Cottle, J.M., Lederer, G., & Ahmad, T., 2012. Timing of metamorphism, melting and exhumation of the Leo Pargil dome, northwest India. Journal of Metamorphic Geology 30, 769–791. http://dx.doi.org/10.1111/j.1525-1314.2012.00998x.
Lavier, L.L., & Buck, W.R., 2002. Half graben versus large-offset low-angle normal fault: the importance of keeping cool during normal faulting. Journal of Geophysical Research 107, 2122. http://dx.doi.org/10.1029/2001JB000513.
Lee, J.-Y., Marti, K., Severinghaus, J.P., Kawamura, K., Yoo, H.-S., Lee, J.B., & Kim, J.S., 2006. A redetermination of the isotopic abundances of atmospheric Ar. Geochimica et Cosmochimica Acta 70, 4507–4512.
Lin, W., Faure, M., Monie, P., Scharer, U., & Panis, D., 2008. Mesozoic extensional tectonics in Eastern Asia: the South Liaodong Peninsula Metamorphic Core Complex (NE China). Journal of Geology 116, 134–154.
Lister, G.S., & Baldwin, S.L., 1993. Plutonism and the origin of metamorphic core complexes. Geology 21, 607–610.
Lister, G.S., & Davis, G.A., 1989. The origin of metamorphic core complexes and detachment faults formed during Tertiary continental extension in the northern Colorado River region, U.S.A. Journal of Structural Geology 11, 65–94.
Lister, G.S., Banga, G., & Feenstra, A., 1984. Metamorphic core complexes of Cordilleran type in the Cyclades, Aegean Sea, Greece. Geology 12, 221–225.
Lovera, O.M., Richter, F.M., & Harrison, T.M., 1989. The ^{40}Ar/^{39}Ar thermochronometry for slowly cooled samples having a distribution of diffusion domain sizes. Journal of Geophysical Research 94, 17917–17935.
Luyendyk, B., 1995. Hypothesis for Cretaceous rifting of East Gondwana caused by subducted Slab capture. Geology 23, 373–376.
Luyendyk, B.P., Wilson, D.S., & Siddoway, C.S., 2003. The eastern margin of the Ross Sea Rift in western Marie Byrd Land: crustal structure and tectonic development. Geochemistry, Geophysics, Geosystems http://dx.doi.org/10.1029/2002GC000462.
Malavieille, J., 1993. Late orogenic extension in the mountain belts: insights from the basin and Range and the late Paleozoic Variscan Belt. Tectonics 12, 1115–1130.
McDougall, I., & Harrison, T.M., 1999. Geochronology and Thermochronology by the ^{40}Ar/^{39}Ar Method. Oxford University Press, New York (212 pp.).
McFadden, R., Siddoway, C.S., Teyssier, C., Fanning, C.M., & Kruckenberg, S.C., 2007. Cretaceous oblique detachment tectonics in the Fosdick Mountains, Marie Byrd Land, Antarctica. In: Cooper, A.K., Raymond, C.R., Editorial Team, I.S.A.E.S., et al. (Eds.), Antarctica. A Keystone in a Changing World - Online Proceedings of the 10th ISAES. USGS Open-File Report 2007–1047, Short Research Paper 046 (6 pp.).
McFadden, R.R., Siddoway, C.S., Teyssier, C., & Fanning, C.M., 2010a. Cretaceous oblique extensional deformation and magma accumulation in the Fosdick Mountains migmatite-cored gneiss dome, West Antarctica. Tectonics 29. http://dx.doi.org/10.1029/2009TC002492 (TC4022).
McFadden, R.R., Teyssier, C., Siddoway, C.S., Whitney, D.L., & Fanning, C.M., 2010b. Oblique dilation, melt transfer, and gneiss dome emplacement. Geology 38, 375–378.
Min, K., Mundil, R., Renne, P.R., & Ludwig, K.R., 2000. A test for systematic errors in 40Ar/39Ar geochronology through comparison with U/Pb analysis of a 1.1-Ga rhyolite. Geochimica et Cosmichimca Acta 64, 73–98.
Mortimer, N., Tulloch, A.J., Spark, R.N., Walker, N.W., Ladley, E., Allibone, A., & Kimbrough, D.L., 1999. Overview of the Median Batholith, New Zealand: a new interpretation of the geology of the Median Tectonic Zone and adjacent rocks. Journal of African Earth Sciences 29, 257–268.
Mortimer, N., Hoernle, K., Hauff, F., Palin, J.M., Dunlap, W.J., Werner, R., & Faure, K., 2006. New constraints on the age and evolution of the Wishbone Ridge, southwest Pacific Cretaceous microplates, and Zealandia-West Antarctica breakup. Geology 3, 185–188.
Muir, R.J., Ireland, T.R., Weaver, S.D., Bradshaw, J.D., Waight, T.E., Jongens, R., & Eby, G.N., 1997. SHRIMP U–Pb geochronology of Cretaceous magmatism in northwest Nelson-Westland, South Island, New Zealand, New Zealand. Journal of Geology and Geophysics 40, 453–463.
Muir, R., Ireland, T.R., Weaver, S.D., Bradshaw, J.D., Evans, J.A., Eby, G.N., & Shelley, D., 1998. Geochronology and geochemistry of a Mesozoic magmatic arc system, Fiordland, New Zealand. Journal of the Geological Society of London 155, 1037–1053.
Mukasa, S.B., & Dalziel, I.W., 2000. Marie Byrd Land, West Antarctica: evolution of Gondwana's Pacific margin constrained by zircon U–Pb geochronology and feldspar common-Pb isotopic compositions. Geological Society of America Bulletin 112, 611–627.
Mulch, A., Teyssier, C., Cosca, M.A., & Vennemann, T.W., 2006. Thermomechanical analysis of strain localization in a ductile detachment zone. Journal of Geophysical Research 111 (B12405).
Norlander, B., Whitney, D., Teyssier, C., & Vanderhaeghe, O., 2002. Partial melting and decompression of the Thor-Odin dome, Shuswap metamorphic core complex, Canadian Cordillera. Lithos 61, 103–125.
Pankhurst, R.J., Weaver, S.D., Bradshaw, J.D., Storey, B.C., & Ireland, T.R., 1998. Geochronology and geochemistry of pre-Jurassic superterranes in Marie Byrd Land, Antarctica. Journal of Geophysical Research 103, 2529–2547.
Rey, P., Teyssier, C., & Whitney, D.L., 2009a. Extension rates, crustal melting, and core complex dynamics. Geology 37, 391–394. http://dx.doi.org/10.1130/G25460A.1.
Rey, P., Teyssier, C., & Whitney, D.L., 2009b. The role of partial melting and extensional strain rates in the development of metamorphic core complexes. Tectonophysics 477, 135–144. http://dx.doi.org/10.1016/j.tecto.2009.03.010.
Richard, S.M., 1992. Structure and Cooling History of the Fosdick Metamorphic Complex, Marie Byrd Land, West Antarctica. In: Yoshida, Y., et al. (Eds.), Recent Progress in Antarctic Earth Science. Terra Publications, Tokyo, Japan, pp. 289–294.
Richard, S.M., Smith, C.H., Kimbrough, D.L., Fitzgerald, P.G., Luyendyk, B.P., & McWilliams, M.O., 1994. Cooling history of the northern Ford Ranges, Marie Byrd Land, West Antarctica. Tectonics 13, 837–857.
Roger, F., Teyssier, C., Respaut, J., Rey, P.F., Jolivet, M., Whitney, D.L., Paquette, J., & Brunel, M., 2015. Timing of formation and exhumation of the Montagne Noire double dome, French Massif Central. Tectonophysics 640–641, 53–69.
Saito, S., Brown, M., Korhonen, F.J., McFadden, R.R., & Siddoway, C.S., 2013. Petrogenesis of Cretaceous mafic intrusive rocks, Fosdick Mountains, West Antarctica: melting of the sub-continental arc mantle along the Gondwana margin. Gondwana Research 23, 1567–1580.
Scott, J.M., & Cooper, A.F., 2006. Early Cretaceous extensional exhumation of the lower crust of a magmatic arc: evidence from the Mount Irene Shear Zone, Fiordland, New Zealand. Tectonics 25. http://dx.doi.org/10.1029/2005TC001890.
Siddoway, C.S., 2008. Tectonics of the West Antarctic rift system: new light on the history and dynamics of distributed intracontinental extension. In: Cooper, A.K., et al. (Eds.), Antarctica: A Keystone in a Changing World. National Academy of Sciences.
Siddoway, C.S., & Fanning, C.M., 2009. Paleozoic tectonism on the East Gondwana margin: evidence from SHRIMP U–Pb zircon geochronology of a migmatite–granite complex in West Antarctica. Tectonophysics http://dx.doi.org/10.1016/j.tecto.2009.04.021.
Siddoway, C.S., Baldwin, S.L., Fitzgerald, P.G., Fanning, C.M., & Luyendyk, B.P., 2004a. Ross Sea mylonites and the timing of intracontinental extension within the West Antarctic rift system. Geology 32, 57–60.
Siddoway, C.S., Richard, S.M., Fanning, C.M., & Luyendyk, B.P., 2004b. Origin and emplacement of a middle Cretaceous gneiss dome, Fosdick Mountains, West Antarctica. In: Whitney, D.L., Teyssier, C., Siddoway, C.S. (Eds.), Gneiss Domes in Orogeny. Geological Society of America Special Paper 380, pp. 267–294.
Siddoway, C.S., Sass III, L.C., & Esser, R., 2005. Kinematic history of Marie Byrd Land terrane, West Antarctica: direct evidence from Cretaceous mafic dykes. In: Vaughan, A., et al. (Eds.), Terrane processes at the margin of Gondwana. Geological Society of London Special Publications 246, pp. 417–438.
Smith, C.H., 1992. Cordierite gneisses and high temperature metamorphism in the Fosdick Mountains, West Antarctica, with implications for breakup processes in the Pacific sector of the Mesozoic Gondwana margin (PhD Thesis), University of California, Santa Barbara (318 pp.).
Storey, B., Leat, T., Weaver, S.D., Pankhurst, R.J., Bradshaw, J.D., & Kelley, S., 1999. Mantle plumes and Antarctica–New Zealand rifting: evidence from mid-Cretaceous mafic dykes. Journal of the Geological Society of London 156, 659–671.

Sutherland, R., & Hollis, C., 2001. Cretaceous demise of the Moa plate and strike–slip motion at the Gondwana margin. Geology 29, 279–282. http://dx.doi.org/10.1130/0091-7613(2001)029<0279:CDOTMP>2.0CO;2.

Thomson, S.N., Reiners, P.W., Hemming, S.R., & Gehrels, G.E., 2013. The contribution of glacial erosion to shaping the hidden landscape of East Antarctica. Nature Geoscience 6, 203–207. http://dx.doi.org/10.1038/ngeo1722.

Tirel, C., Brun, J.-P., & Sokoutis, D., 2006. Extension of thickened and hot lithospheres: inferences from laboratory modeling. Tectonics 25, TC1005. http://dx.doi.org/10.1029/2005TC001804.

Tirel, C., Brun, J.-P., & Burov, E., 2008. Dynamics and structural development of metamorphic core complexes. Journal of Geophysical Research 113, B04403. http://dx.doi.org/10.1029/2005JB003694.

Toraman, E., Teyssier, C., Whitney, D.L., Fayon, A.K., Thomson, S.N., & Reiners, P.W., 2014. Low-temperature thermochronologic record of Eocene migmatite dome emplacement and late Cenozoic landscape development, Shuswap core complex, British Columbia. Tectonics 33.

Tulloch, A.J., & Kimbrough, D.L., 1989. The Paparoa metamorphic core complex, New Zealand: Cretaceous extension associated with fragmentation of the Pacific margin of Gondwana. Tectonics 8, 1217–1234.

Tulloch, A.J., & Kimbrough, D.L., 2003. Paired plutonic belts in convergent margins and the development of high Na, Al, Sr, low Y magmatism: the Peninsular Ranges Batholith of California and the Median Batholith of New Zealand. In: Johnson, S.E., et al. (Eds.), Tectonic evolution of the northwestern Mexico and the southwestern USA. Geological Society of America Special Publication 374, pp. 275–295.

Tulloch, A.J., Beggs, M., Kula, J., Spell, T., & Mortimer, N., 2006. Cordillera Zealandia, the Sisters Shear Zone and their influence on the early development of the Great South Basin, Field Developments and Production/Keynote paper.

Vanderhaeghe, O., Burg, J.P., & Teyssier, C., 1999. Exhumation of migmatites in two collapsed orogens: Canadian Cordillera and French Variscides. In: Ring, U., Brandon, U., Lister, G.S., Willett, S.D. (Eds.), Exhumation Processes. Normal Faulting, Ductile Flow and Erosion. Geological Society London Special Publication 154, pp. 181–204.

Vaughan, A.P.M., 1995. Circum-Pacific mid-Cretaceous deformation and uplift: a superplume-related event. Geology 23, 491–494.

Vaughan, A.P.M., Eagles, G., & Flowerdew, M.J., 2012. Evidence for a two-phase Palmer Land event from crosscutting structural relationships and emplacement timing of the Lassiter Coast Intrusive Suite, Antarctic Peninsula: implications for mid-Cretaceous Southern Ocean plate configuration. Tectonics 31. http://dx.doi.org/10.1029/2011TC003006.

Villa, I., 1998. Isotopic closure. Terra Nova 10, 42–47.

Watson, E.B., Wark, D.A., & Thomas, J.B., 2006. Crystallization thermometers for zircon and rutile. Contributions to Mineralogy and Petrology 151, 413–433.

Weaver, S.D., Adams, C.J., Pankhurst, R.J., & Gibson, I.L., 1992. Granites of Edward VII Peninsula, Marie Byrd Land: anorogenic magmatism related to Antarctic-New Zealand rifting. In: Brown, E., Chappell, B.W. (Eds.), Proceedings of the Second Hutton Symposium on the Origin of Granites and Related Rocks. Transactions of the Royal Society Edinburgh - Earth Sciences, pp. 281–290.

Weaver, S.D., Storey, B.C., Pankhurst, R.J., Mukasa, S.B., Divenere, V., & Bradshaw, J.D., 1994. Antarctic-New Zealand rifting and Marie Byrd Land lithospheric magmatism linked to ridge subduction and mantle plume activity. Geology 22, 811–814.

Whitney, D.L., Teyssier, C., & Fayon, A.K., 2004. Isothermal decompression, partial melting and exhumation of deep continental crust. In: Grocott, J., McCaffrey, K.J.W., Taylor, G., Tikoff, B. (Eds.), Vertical Coupling and Decoupling in the Lithosphere. Geological Society of London Special Publication 227, pp. 313–326.

Whitney, D.L., Teyssier, C., Rey, P., & Buck, W.R., 2013. Continental and oceanic core complexes. Geological Society of America Bulletin 125, 273–298. http://dx.doi.org/10.1130/B30754.1.

Willigers, B.J.A., Krogstad, E.J., & Wijbrans, J.R., 2001. Comparison of thermochronometers in a slowly cooled granulite terrain: Nagssugtqidian Orogen, West Greenland. Journal of Petrology 42, 1729–1749.

Wu, F.Y., Yang, J.H., Wilde, S.A., & Zhang, X.O., 2005. Geochronology, petrogenesis and tectonic implications of Jurassic granites in the Liaodong Peninsula, NE China. Chemical Geology 221, 127–156.

Yakymchuk, C., Siddoway, C.S., Fanning, C.M., McFadden, R.R., Korhonen, F.J., & Brown, M., 2013a. Anatectic reworking and differentiation of continental crust along the active margin of Gondwana: a zircon Hf-O perspective from West Antarctica. Geological Society of London, Special Publication 383. http://dx.doi.org/10.1144/SP383.7.

Yakymchuk, C., Brown, M., Ivanic, T.J., & Korhonen, F.J., 2013b. Leucosome distribution in migmatitic paragneisses and orthogneisses: a record of self-organized melt migration and entrapment in a heterogeneous partially molten crust. Tectonophysics 603, 136–154.

Yang, J.H., Wu, F.Y., Chung, S.L., Lo, C.H., Wilde, S.A., & Davis, G.A., 2007. Rapid exhumation and cooling of the Liaonan metamorphic core complex: inferences from $^{40}Ar/^{39}Ar$ thermochronology and implications for late Mesozoic extension in the eastern North China Craton. Geological Society of America Bulletin 119, 1405–1414. http://dx.doi.org/10.1130/B26085.1.